Accurate and Omnidirectional UWB Radar Imaging Algorithm With RPM Method Extended to Curvilinear Scanning Model

Yoriaki Abe, Shouhei Kidera, *Associate Member, IEEE*, and Tetsuo Kirimoto, *Senior Member, IEEE*

***Abstract*—Ultrawideband pulse radars are a promising technology for high-quality imaging sensors for rescue robots in the near field because they have the advantage of high range resolution. We have already proposed the accurate and fast imaging algorithm as range point migration (RPM), which employs the direction of arrival (DOA) with the global characteristic of the multiple observed ranges. However, this algorithm assumes the line scanning of an omnidirectional antenna and limits the imaging range. To overcome this limitation, this letter derives an extended RPM method, which accomplishes omnidirectional imaging and accurate target positioning. As a false-image-reduction scheme in this method, this letter introduces a postprocessing algorithm, which constrains the searching range for DOA estimation by using the initial RPM image. The results of numerical simulations, including noisy situations, show that the proposed method accomplishes accurate and omnidirectional imaging on the order of 1/100 wavelength and enhances the imaging range while avoiding false images.**

***Index Terms*—Curvilinear scanning, false-image reduction, omnidirectional imaging, range point migration (RPM), ultrawideband (UWB) pulse radars.**

I. Introduction

ULTRAWIDEBAND (UWB) pulse radars have great potential in near-field measurement even in critical situations such as disaster sites, where an optical measurement is barely applicable due to dusty air or dark smog. They also have a definitive advantage for high-range-resolution imaging. In recent years, various types of radar imaging algorithms based on data synthesis, such as synthetic aperture radar (SAR) [1], time-reversal algorithms [2], [3], and range migration methods [4], [5], have been proposed. However, their computational burdens often become impractically large, and they are then unsuitable for real-time applications such as robotic sensors. On the other hand, the high-speed imaging algorithm called the Shape Estimation Algorithm based on BST and Extraction of Directly scattered waves (SEABED) achieves direct and nonparametric imaging based on reversible transforms between the time delay and target boundary [6]. However, SEABED requires the accurate extraction of the so-called quasi-wavefront, which is connected by multiple range points, and distorts the image, particularly for the multiple or complex-shaped targets. On the contrary, we have already proposed the accurate and fast imaging algorithm, range point migration (RPM), which uses observed range points and their amplitudes to estimate the direction of arrival (DOA) [7]. Because this method is based on direct group mapping from observed ranges to target points, it does not require range connection and substantially resolves the inaccuracy in estimating complex target shapes. In addition, an accurate range extraction method using a frequency-domain interferometer has been proposed [8], which is applicable to more complex-shaped targets. Conversely, the methods in [7] and [8], based on the original RPM, assume linear scanning and are not suitable for omnidirectional imaging, which is required for a moving robot application. This is because the methods often produce many false images, even if all range points are accurately extracted.

First, this letter extends the conventional RPM so that it is suitable for the curvilinear scanning of an antenna and omnidirectional imaging. Then, we introduce an example using the extended RPM, indicating that it creates false images far from the actual target boundary. To enhance the accuracy of the imaging, a false-image-reduction algorithm is incorporated, which constrains the searching range for the DOA estimation using the initial target points obtained by the RPM. This constraint is based on the unique property that the spatial density of target points corresponding to a false image is considerably different from that corresponding to actual points. The results in numerical simulations assuming the multiple targets and noisy situations prove that the proposed method successfully suppresses the false images and accomplishes accurate target imaging on the order of 1/100 wavelength, even for a curvilinear scan trajectory.

II. System Model

Fig. 1 shows the system model. It assumes that targets have arbitrary shapes with clear boundaries. It employs a monostatic radar system, where an omnidirectional antenna is scanned along an arbitrary curve. It assumes that targets are not included in the observation domain. We also assume that the propagation speed of the radio wave is known and constant. We use a monocycle pulse as the transmitting current. The space in which the targets and antenna are located is expressed by the parameters x and z. The parameters are normalized by λ, which is the central wavelength of the pulse. $s'(X, Z, t)$ is defined as the electric field received at the antenna location $(x, z) = (X, Z)$ at time t. $s(X, Z, t)$ is the output of the Wiener filter, whose definition and filtering procedure are described in [7]. $s(X, Z, t)$ is converted to $s(X, Z, R')$ using the useful

Manuscript received December 28, 2010; revised April 27, 2011 and July 5, 2011; accepted July 11, 2011. Date of publication August 22, 2011; date of current version December 23, 2011.

The authors are with the Graduate School of Informatics and Engineering, The University of Electro-Communications, Tokyo 182-8585, Japan (e-mail: abe@secure.ee.uec.ac.jp; kidera@ee.uec.ac.jp; kirimoto@ee.uec.ac.jp).

Digital Object Identifier 10.1109/LGRS.2011.2162313

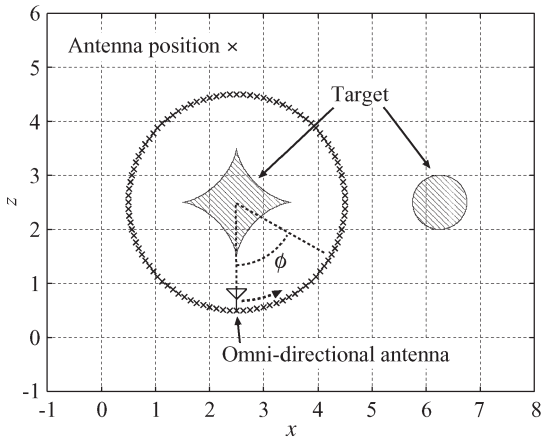

Fig. 1. System model.

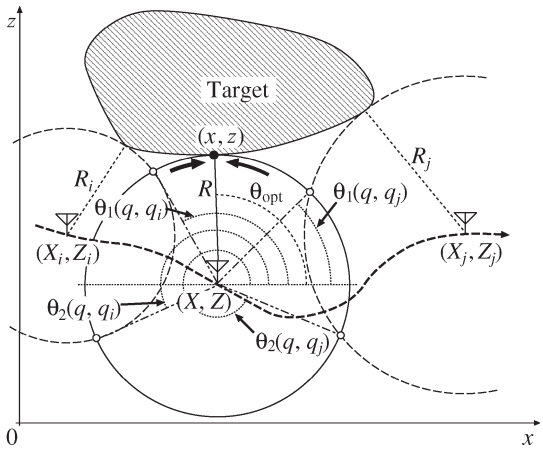

Fig. 2. Relationship between the target boundary and the intersection points of the circles.

conversion $R' = c_0 t/2\lambda$, where c_0 is the speed of the radio wave. The group of the so-called range points (X, Z, R) is extracted from the local peaks of $s(X, Z, R')$ as

$$\frac{\partial s(X,Z,R')}{\partial R'} = 0$$
$$s(X,Z,R') \geq \alpha \ \max s(X,Z,R'). \tag{1}$$

The parameter $\alpha > 0$ is empirically determined.

III. Proposed Method

A. RPM Algorithm for Curvilinear Scanning Model

The RPM has been proposed as a conventional radar algorithm, which achieves accurate and high-resolution imaging even for extremely complex-shaped targets. However, the conventional RPM assumes the line scanning of an omnidirectional antenna and limits the imaging range. This section extends the RPM so that it is suitable for curvilinear scanning and omnidirectional imaging. The RPM algorithm is based on the simple principle that a target boundary point should exist on a circle, with a center at the antenna position (X, Z) and radius R. Thus, each point (x, z) can be calculated using the corresponding DOA. Although this algorithm basically assumes the linear scanning of the antenna, it can be readily applied to arbitrary curvilinear scanning and realizes omnidirectional imaging by calculating the intersection points of the full circles. For omnidirectional imaging, the evaluation function for DOA as $f_k(\theta; \boldsymbol{q}, \boldsymbol{q_i})$ is extended as

$$f_k(\theta; \boldsymbol{q}, \boldsymbol{q_i}) = \exp\left[-\frac{\{\theta - \theta_k(\boldsymbol{q}, \boldsymbol{q}_i)\}^2}{2\sigma_\theta^2}\right], \qquad k = 1, 2 \tag{2}$$

where $\boldsymbol{q} = (X, Z, R)$ and $\boldsymbol{q_i} = (X_i, Z_i, R_i)$ are defined and the constant σ_θ is empirically determined. $\theta_k(\boldsymbol{q}, \boldsymbol{q_i})$ denotes the angle from the x-axis to the intersection points of the circles, with parameters (X, Z, R) and (X_i, Z_i, R_i). The two intersection points for each pair of circles are discriminated by the index k. Fig. 2 shows the relationship between the intersection points of the circles and the DOA for the actual scattering point. The evaluation values $F_k(\theta; \boldsymbol{q})$ for the DOA estimation are defined as

$$F_k(\theta; \boldsymbol{q}) = \sum_{i=1}^{N_q} s(X_i, Z_i, R_i) f_k(\theta; \boldsymbol{q}, \boldsymbol{q}_i) \times \exp\left[-\frac{(X - X_i)^2 + (Z - Z_i)^2}{2\sigma_F^2}\right], \qquad k = 1, 2 \tag{3}$$

where N_q is the total number of the range points and the constant σ_F is empirically determined. As the antenna position (X_i, Z_i) moves to (X, Z), its intersection point converges to the actual scattering point, and consequently, $F_k(\theta; \boldsymbol{q})$ evolves around the true DOA. Since it is difficult to determine whether $F_1(\theta; \boldsymbol{q})$ or $F_2(\theta; \boldsymbol{q})$ should be considered, the optimum DOA for each $\boldsymbol{q}$ is calculated as

$$\theta_{\text{opt}} = \arg\max_{\theta \in \Theta} \{F_1(\theta; \boldsymbol{q}) + F_2(\theta; \boldsymbol{q})\} \tag{4}$$

where $\Theta = \{\theta | 0 \leq \theta < 2\pi\}$. The target boundary (x, z) for each range point (X, Z, R) is expressed as

$$\left.\begin{aligned} x &= X + R\cos\theta_{\text{opt}} \\ z &= Z + R\sin\theta_{\text{opt}} \end{aligned}\right\}. \tag{5}$$

By calculating all the intersection points of the circles, this extended RPM algorithm can be applied to curvilinear scan trajectories and accomplish omnidirectional imaging. However, neither of the two intersection points of the circles corresponds to the actual target point, and a misselection of these points then causes false images.

B. False-Image-Reduction Scheme

To resolve the aforementioned problem, this letter derives a postprocessing algorithm, which constrains the searching range for the DOA estimation. This scheme is based on the unique characteristic of the RPM that, if the estimated target point is close to an actual target boundary, the neighboring region around this point should be also reconstructed from different antenna locations. On the contrary, in the case of the false image, this characteristic is rarely satisfied. Consequently, the

spatial density of the target points around the actual target boundary is comparatively higher than that for the false images. For the searching range constraint, the following function $g(\theta, \theta_l; X, Z)$ is introduced as

$$g(\theta, \theta_l; X, Z) = \exp\left[-\frac{(\theta - \theta_l)^2}{2\sigma_g^2}\right], \qquad l = 1, \ldots, N_T \tag{6}$$

where σ_g is constant, N_T is the total number of the estimated target points, which are obtained by the RPM, and θ_l denotes the angle from the x-axis to the point $(x_l - X, z_l - Z)$. Then, the evaluation function $G(\theta; X, Z)$ for the searching range is introduced as

$$G(\theta; X, Z) = \sum_{l=1}^{N_T} g(\theta, \theta_l; X, Z). \tag{7}$$

$G(\theta; X, Z)$ takes a large value at the angle where sufficient numbers of estimated points exist. The searching range for the DOA at (X, Z) is determined as

$$\Theta(X, Z) = \left\{\theta | G(\theta; X, Z) \geq \gamma \max_{\theta} G(\theta; X, Z)\right\} \tag{8}$$

where the constant γ is empirically determined. To suppress false images, we recalculate θ_{opt} for each range point (X, Z, R) using the searching range of $\Theta(X, Z)$

$$\theta_{\text{opt}} = \arg \max_{\theta \in \Theta(X,Z)} \left\{F_1(\theta; \boldsymbol{q}) + F_2(\theta; \boldsymbol{q})\right\}. \tag{9}$$

It should be noted that the constant σ_g is determined based on the sampling interval of the antenna. This is because the interval of the target points becomes close to that of the antenna locations due to the characteristic of the RPM, as previously mentioned. Hence, if the σ_g in (6) is too small compared with the sampling interval of the antenna, the $G(\theta; X, Z)$ in (7) does not grow effectively in the true DOA. On the contrary, if σ_g is too large, $G(\theta; X, Z)$ grows over a wide range, and then, the constraint of the searching range does not work correctly. The procedure of the proposed method is as follows.

Step 1) A set of target points is obtained as $\mathcal{T}_{\text{rpm}} = \{(x_l, z_l) | l = 1, 2, \ldots, N_T\}$ in (4) and (5).

Step 2) Using target points $\mathcal{T}_{\text{rpm}}$, the searching range $\Theta(X, Z)$ is calculated in (6)–(8) for each range point (X, Z, R).

Step 3) For each range point (X, Z, R), the target points are updated using (5) and (9), with the constrained searching range as $\Theta(X, Z)$, and are added to $\mathcal{T}_{\text{temp}} = \{(x_m, z_m) | m = 1, 2, \ldots, N_T\}$.

Step 4) Remove the target points in $\mathcal{T}_{\text{temp}}$ that satisfy

$$\sqrt{(X - x_m)^2 + (Z - z_m)^2} \leq \kappa \min_j R_j \tag{10}$$

where $\kappa \leq 1$ and R_j denotes the jth range points observed at the same antenna location at (X, Z), and we finally obtain the target points as $\mathcal{T}_{\text{prop}} = \{(x_n, z_n) | n = 1, 2, \ldots, N_T'\}$, where N_T' is the remaining number of target points.

Step 4) suppresses false images caused by random noise because there should be no target points inside the circle whose center is the antenna position and radius is the shortest observed range at the position. It should be noted that the proposed method not only decreases the number of false images but also increases the number of accurate target points by recalculating the DOA. It then achieves accurate omnidirectional imaging without using *a priori* knowledge of target locations.

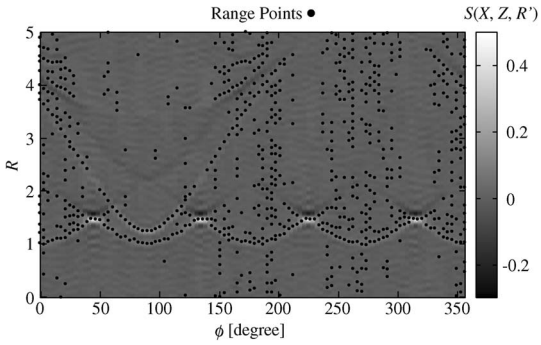

Fig. 3. Output of the Wiener filter and the extracted range points for $S/N = 30$ dB.

IV. Numerical Simulations

This section investigates the imaging performance for each method. We assume two targets with clear boundaries, as shown in Fig. 1. One target has an asteroidal boundary and is expressed as $(x - 2.5)^{2/3} + (z - 2.5)^{2/3} = 1$, and the other target has a circular boundary and is expressed as $(x - 6.25)^2 + (z - 2.5)^2 = 0.5^2$. The conductivity and relative permittivity of the targets are set to 1.0×10^6 S/m and 1.0, respectively. An omnidirectional antenna is scanned along the circle whose center is $(x, z) = (2.5, 2.5)$ and radius is 2λ. Any type of curvilinear scan trajectory, even if it is not differentiable, can, in principle, be used instead. The finite-difference time-domain method is used for the calculation of the received signals. Gaussian noises are added to the received signals, and in this case, $S/N = 30$ dB. Here, the S/N is defined as the ratio of the peak instantaneous signal power to the averaged noise power after applying the matched filter. Fig. 3 shows the output of the Wiener filter and the extracted range points (X, Z, R), where ϕ denotes the angle as shown in Fig. 1. Fig. 4 shows the image estimated by the proposed method before false-image reduction. $\sigma_\theta = \pi/25$, $\sigma_F = 0.5\lambda$, $\alpha = 0.3$, and $\beta = 0.2$ are set. This result indicates that the proposed algorithm creates target points along the actual boundary even when using the curvilinear scanning of the antenna. However, it also shows that there are some false images outside the circular scan trajectory. These false images appear when the intersection points of the circles converge to the opposite side of the actual target. On the other hand, Fig. 5 shows the image estimated after the false-image reduction is applied. $\sigma_g = \pi/10$, $\gamma = 0.3$, and $\kappa = 0.8$ are set. It is obvious from the result that this postprocessing significantly suppresses the false images and increases the number of target points close to the actual boundary.

For a comparison, the SAR method extended to the near field [7] is evaluated. Fig. 6 shows the example of the SAR of the same target in Fig. 1. Although this method focuses on the image around the actual boundary, it creates many unnecessary images far from the actual boundary. These false images are basically caused by the same effects originated in the extended RPM method. Furthermore, the spatial resolution of the SAR

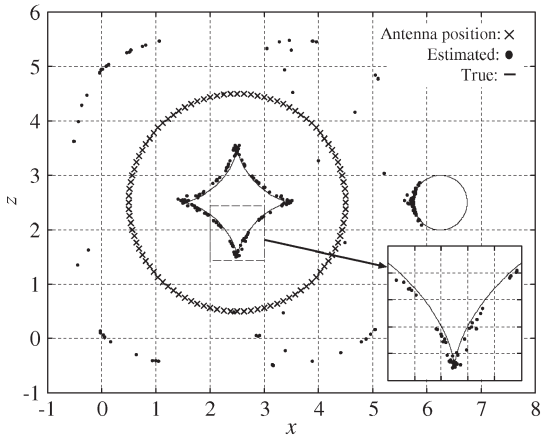

Fig. 4. Estimated image with the proposed method before false-image reduction for $S/N = 30$ dB.

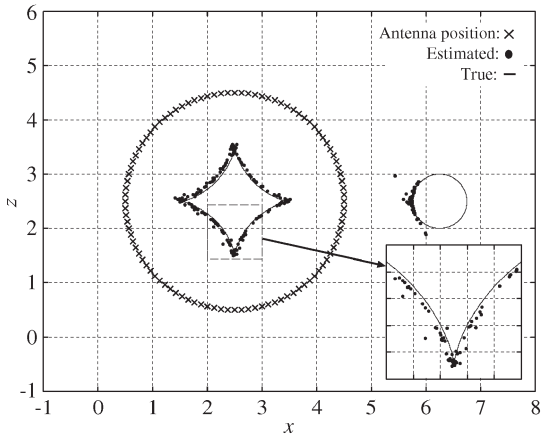

Fig. 5. Estimated image with the proposed method after false-image reduction for $S/N = 30$ dB.

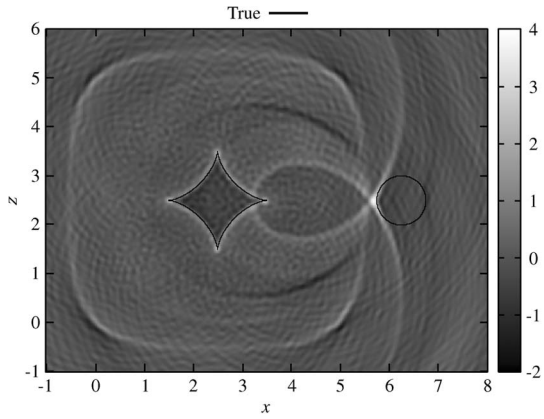

Fig. 6. Estimated image with the SAR for $S/N = 30$ dB.

is strictly determined by half a pulsewidth, even if an infinite aperture size is given, which is often not sufficient to identify the edge region.

For a quantitative evaluation of the accuracy, $\epsilon(\boldsymbol{x}_e^i)$ is introduced as

$$\epsilon\left(\boldsymbol{x}_e^i\right) = \min\left\|\boldsymbol{x} - \boldsymbol{x}_e^i\right\|, \qquad (i = 1, 2, \ldots, N_T) \qquad (11)$$

where $\boldsymbol{x}$ and $\boldsymbol{x}_e^i$ express the location of the true target point and the estimated point, respectively. N_T is the total number

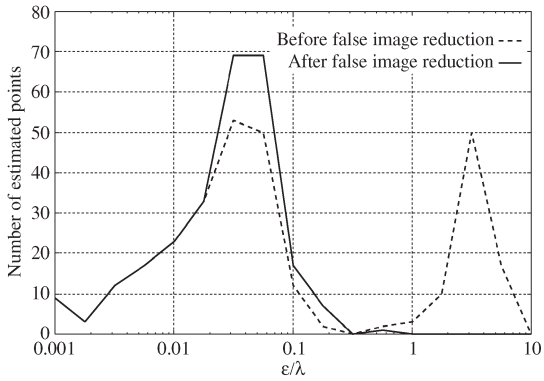

Fig. 7. Error distribution for the proposed method before and after false-image reduction.

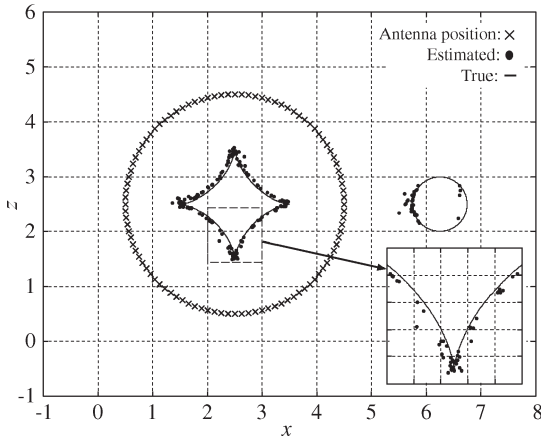

Fig. 8. Estimated image with the proposed method after image reduction for $S/N = 30$ dB.

of $\boldsymbol{x}_e^i$'s. Fig. 7 shows the plots of the number of estimated points for each value of ϵ. The N_T for each result is 296 for the proposed method before false-image reduction, and it is 260 for the proposed method after false-image reduction. This figure reveals that the number of estimated points with $\epsilon \geq 1.0\lambda$ for the extended RPM algorithm becomes large due to the false image, while the proposed method completely suppresses the estimated points with such errors. On the contrary, the number of estimated points with $\epsilon \leq 0.1\lambda$ increases with the proposed method. This result appeals as a noticeable advantage in that the proposed method not only removes the false-image points but also increases the points around the actual boundary using accurate DOA recalculation. The mean values of ϵ as $\bar{\epsilon}$ for each result are about 0.75λ for the extended RPM algorithm and about 0.029λ for the proposed algorithm. As a reference, the image estimated by the proposed method for an $S/N = 20$ dB is shown in Fig. 8. This evaluation shows that the proposed method is still accurate for lower S/N ratios.

Fig. 9 shows the relationship between $\bar{\epsilon}$ and S/N for the extended RPM algorithm and the proposed algorithm. This figure shows that the value of $\bar{\epsilon}$ for the proposed algorithm is considerably lower than that of the extended RPM algorithm in the case of $S/N \geq 20$ dB. However, in the case of $S/N \leq 15$ dB, the accuracy of the proposed algorithm deteriorates. This is because the number of false images for the lower S/N increases due to random noise, and there is then no significant difference in the spatial density between the actual and false points. This figure

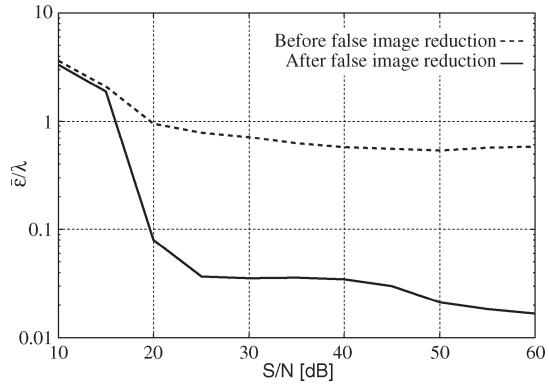

Fig. 9. Relationship between $\bar{\epsilon}$ and S/N for the proposed method before and after false-image reduction.

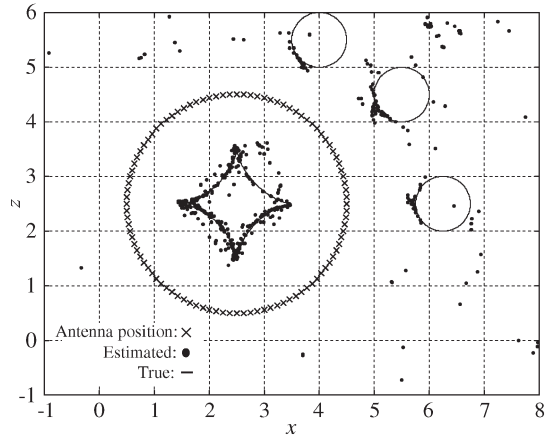

Fig. 10. Estimated image with the proposed method in a multiple scattering environment for $S/N = 30$ dB.

also verifies that the proposed method accomplishes accurate target imaging within 0.03λ over $S/N \geq 25$ dB. Although this method apparently requires high S/N levels to retain accuracy, the definition of the S/N ratio considers the locality both in the frequency domain and in the time domain because it strictly estimates UWB pulse power, and Kidera *et al.* [7] indicate that the actual UWB radar system can achieve this level of S/N under the assumption of near-field measurement.

To discuss the mutual effects due to multiple scattering, Fig. 10 shows another example using the proposed method for the case of two more circular targets which are added to the previous case. The S/N level is 30 dB. This figure indicates that false images can be recognized far from the actual target locations because the range points extracted from the multiple scattering echoes produce incorrect images. The proposed method cannot deal with this type of false image, and our future studies will remove these images based on an approach such as that in [6].

The imaging range of the proposed method is assumed to be more than a wavelength distance from the antenna locations to avoid the mutual coupling effect between the antenna and targets. Furthermore, the proposed method is applicable to the far-field area if sufficient accuracy for range extraction is obtained. Thus, the imaging range is mainly determined by the S/N levels, which is generally common for any conventional methods.

Note that the antenna scan trajectory plays an essential role for the reconstructible area of the target boundary because strong echoes are observed only from the target boundary perpendicular to the line of sight [7]. Thus, the curvilinear scan trajectory here is set to surround the asteroidal target so that the overall shape of this target can be obtained. Furthermore, if the target has deep concave edges, the antenna may need to be scanned near the concave edge region to observe the scattered signals. Moreover, this is an inherent and common property in all the conventional and proposed approaches.

As an additional remark, since this evaluation employs *a priori* knowledge as to the possible observation domain, this domain should be sequentially estimated by employing the observed range data or the previously obtained images in realistic situations. As one of the effective schemes for this extension, the first arrival range can be employed to determine the next possible antenna location, and this idea is similar to the false-image-reduction scheme provided in Step 4) of the procedure of the proposed method. This is because it is a generally acceptable fact that the inside area of the circle, whose radius is the first range and center is (X, Y), should not include the target existing area and can offer the next possible observation domain. However, this problem will be treated in our future work.

V. Conclusion

In this letter, we have first extended the conventional RPM so that it is suitable for the curvilinear scanning of an antenna and omnidirectional imaging. Then, we have introduced an example using the extended RPM, indicating that it creates false images far from the actual target boundary. To overcome this difficulty, a novel image-recovering algorithm has been proposed, which constrains the searching range for the DOA estimation using initially estimated target points with the RPM method. The results in numerical simulations including noisy situations show that the proposed method accomplishes accurate target imaging on the order of 1/100 wavelength, even with a curvilinear scan trajectory.

References

[1] D. L. Mensa, G. Heidbreder, and G. Wade, "Aperture synthesis by object rotation in coherent imaging," *IEEE Trans. Nucl. Sci.*, vol. NS-27, no. 2, pp. 989–998, Apr. 1980.

[2] A. J. Devaney, "Time reversal imaging of obscured targets from multistatic data," *IEEE Trans. Antennas Propag.*, vol. 53, no. 5, pp. 1600–1610, May 2005.

[3] E. A. Marengo, F. K. Gruber, and F. Simonetti, "Time-reversal MUSIC imaging of extended targets," *IEEE Trans. Image Process.*, vol. 16, no. 8, pp. 1967–1984, Aug. 2007.

[4] J. Song, Q. H. Liu, P. Torrione, and L. Collins, "Two-dimensional and three dimensional NUFFT migration method for landmine detection using ground-penetrating radar," *IEEE Trans. Geosci. Remote Sens.*, vol. 44, no. 6, pp. 1462–1469, Jun. 2006.

[5] F. Soldovieri, A. Brancaccio, G. Prisco, G. Leone, and R. Pieri, "A Kirchhoff-based shape reconstruction algorithm for the multimonostatic configuration: The realistic case of buried pipes," *IEEE Trans. Geosci. Remote Sens.*, vol. 46, no. 10, pp. 3031–3038, Oct. 2008.

[6] T. Sakamoto and T. Sato, "A target shape estimation algorithm for pulse radar systems based on boundary scattering transform," *IEICE Trans. Commun.*, vol. E87-B, no. 5, pp. 1357–1365, May 2004.

[7] S. Kidera, T. Sakamoto, and T. Sato, "Accurate UWB radar 3-D imaging algorithm for complex boundary without range points connections," *IEEE Trans. Geosci. Remote Sens.*, vol. 48, no. 4, pp. 1993–2004, Apr. 2010.

[8] S. Kidera, T. Sakamoto, and T. Sato, "Super-resolution UWB radar imaging algorithm based on extended Capon with reference signal optimization," in *Proc. EuCAP*, Apr. 12–16, 2010, pp. 1–5.